



City Research Online

City, University of London Institutional Repository

Citation: Rosti, M. E., Omidyeganeh, M. & Pinelli, A. (2018). Passive control of the flow around unsteady aerofoils using a self-activated deployable flap. *Journal of Turbulence*, 19(3), pp. 204-228. doi: 10.1080/14685248.2017.1314486

This is the accepted version of the paper.

This version of the publication may differ from the final published version.

Permanent repository link: <https://openaccess.city.ac.uk/id/eprint/17323/>

Link to published version: <https://doi.org/10.1080/14685248.2017.1314486>

Copyright: City Research Online aims to make research outputs of City, University of London available to a wider audience. Copyright and Moral Rights remain with the author(s) and/or copyright holders. URLs from City Research Online may be freely distributed and linked to.

Reuse: Copies of full items can be used for personal research or study, educational, or not-for-profit purposes without prior permission or charge. Provided that the authors, title and full bibliographic details are credited, a hyperlink and/or URL is given for the original metadata page and the content is not changed in any way.

City Research Online:

<http://openaccess.city.ac.uk/>

publications@city.ac.uk

RESEARCH ARTICLE

Passive control of the flow around unsteady aerofoils using a self-activated deployable flap

Marco E. Rosti*, Mohammad Omidyeganeh, Alfredo Pinelli
Department of Mechanical and Aeronautical Engineering
City University London
London, U.K.

(Received 00 Month 200x; final version received 00 Month 200x)

Self-activated feathers are used by many birds to adapt their wing characteristics to the sudden change of flight incidence angle (e.g., sudden increase in angle of attack due to gusts or perching manoeuvres). In particular, dorsal feathers are believed to pop up as a consequence of unsteady flow separation and to interact with the flow to palliate the sudden stall breakdown typical of dynamic stall. Inspired by the adaptive character of birds feathers, some authors have envisaged the potential benefits of using of flexible flaps mounted on aerodynamic surfaces to counteract the negative aerodynamic effects associated with dynamic stall. This contribution explores more in depth the physical mechanisms that play a role in the modification of the unsteady flow field generated by a NACA0020 aerofoil equipped with an elastically mounted flap undergoing a specific ramp-up manoeuvre. It is found that it is possible to design flaps that limit the severity of the dynamic stall breakdown by increasing the value of the lift overshoot also smoothing its abrupt decay in time. A detailed analysis on the modification of the unsteady vorticity field due to the flap flow interaction during the ramp-up motion is also provided to explain the more benign aerodynamic response obtained when the flap is in use.

1. Introduction

The demand for helicopters with increased performance and the quest for efficiency improvements in vertical axis wind turbines have prompted further investigations into the dynamic stall that often appears on rotors retreating blades. Dynamic stall is an unsteady phenomenon that takes place on lifting objects in response to time variations of the angle of attack, and it is responsible for dramatic changes in the aerodynamic loads, high vibration affecting the dynamic performance, and occurrence of aeroelastic instability (stall flutter). A considerable number of researches have extensively studied these phenomena in the past [1–6]. Experimental works have mainly focused on unsteady flows over two-dimensional aerofoils undergoing prescribed pitching motions [1–5, 7–11]. McCroskey [2, 3] discovered that the stall is characterised by a lift overshoot, due to the passage of a large scale vortex over the suction side of the aerofoil, followed by a lift breakdown associated with the vortex detachment, and Shih et al. [12] suggested that the main stall vortex is induced by the early boundary layer separation near the leading-edge of the aerofoil, and that full stall occurs when the boundary layer detaches completely from the aerofoil.

High fidelity numerical simulations of dynamic stall in configuration of aeronautical interest are particularly expensive due to the broad range of time and space

*Corresponding author. Email: marco.rosti.1@city.ac.uk

scales involved in the phenomenon. However, conventional turbulence models are known to fail in producing reliable solutions in such complex, out of equilibrium conditions: unsteady, recirculating and locally transitional flow. A general, but somehow outdated review on the numerical simulations of dynamic stall [13–19] can be found in the work of Ekaterinaris and Platzer [20]. Several other works have highlighted the difficulties that RANS calculations encounter when dealing with dynamic stall. In particular, Wang et al. [17] used two variants of the $k - \omega$ model, the standard and the SST one, to simulate the flow at moderate high Reynolds number $Re_c = 10^5$. From a comparison with experimental results, they noticed that the models can not precisely capture the size and position of the dynamic stall vortex. Moreover, the quality of the predictions of the models deteriorate as the angle of attack increases. Dumlupinar and Murthy [18] further investigated the performances of various turbulence models and pointed out that different turbulence closures predict a broad range of different behaviours even in light stall cases. Recently, Rosti et al. [21] performed a DNS of flow around a NACA0020 aerofoil, with the aim of elucidating the physical mechanisms that determine the dynamic stall vortex creation, its evolution along the aerofoil and the subsequent detachment.

Because of the undesirable aerodynamic and structural consequences of dynamic stall, many researchers have focused on the development of control techniques able to palliate such adverse effects. In this framework, a number of different passive and active control techniques [22–25] have been proposed in the past. More recently, researchers have been looking at biomimetic devices to control flow separation on aerofoils at high angle of attack. In particular, it has been observed that birds can overcome certain flight critical conditions, by popping up some of their feathers when flow separation starts to develop on the upper side of their wing [26–28]. It is believed that the feathers lift up may contain backflow thus preventing an abrupt breakdown of aerofoil lift typical of dynamic stall. With the aim of demonstrating the effectiveness of devices mimicking the feathers pop-up, Schatz et al. [29] have shown that a self-activated spanwise flap elastically mounted by the trailing edge of an aerofoil can enhance lift by more than 10% at a chord Reynolds number $Re_c = U_\infty c / \nu$ (U_∞ being the magnitude of the free stream velocity, c the aerofoil chord and ν the kinematic viscosity) in the range of 10^6 . In a related experiment, Schluter [30] has also demonstrated that dynamic stall lift-breakdown is less severe when a similar flap is used.

More recently, Bruecker and Weidner [6] used hairy flaps (i.e., flaps with a thickness much smaller than the plant form sizes) to manipulate the dynamic stall of a wing at moderate Reynolds number $Re_c = 77000$, observing a delay of the dynamic stall. The authors claim that the delay is achieved by both the reduction of the backflow, and by regularising of the shear layer roll-up process. Moreover, they suggest that the onset of the shear layer non-linear growth is delayed via mode-locking of the fundamental instability mode with the motion of the flaps. Rosti et al. [31, 32] performed a DNS of the flow around a NACA0020 aerofoil with a flap mounted via a torsional spring on its suction side at a fixed angle of attack 20° . They found an increase in lift by around 20% when the spring stiffness, geometry and location are properly tuned. Under these conditions, a pulsed jet induced by the flaplet oscillatory movement, that is in turn due to the periodic transit of a large recirculation bubble on the aerofoil suction side, displaces the trailing edge vortices further downstream, away from the wing. The consequences of this downstream displacement of the trailing edge generated vortices, are: a reduction of the downforce generated by these vortices and a regularisation of the shedding cycle that reveals to be much more ordered in time and space when the flaplet is

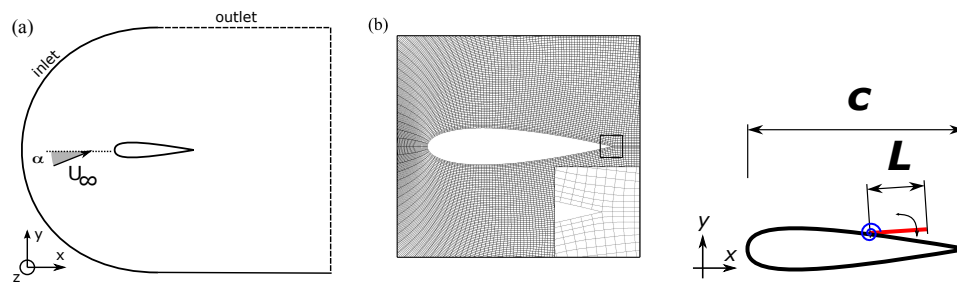


Figure 1. (a) Sketch of the computational domain. (b) Grid in the proximity of the airfoil (nodes are plotted with a skip index of six). The inserted figure is an enlargement of the area surrounding the trailing edge. (c) Sketch of the flap hinged on the suction side of the airfoil through a torsional spring.

activated.

In the present work we focus on the passive control of a NACA0020 airfoil undergoing a ramp-up manoeuvre (angle of attack increased linearly in time from 0° to 20° degrees at an angular speed of $0.12U_\infty/c$), using self-adaptive flaplets elastically mounted on its suction side. The next section introduces the numerical formulation and the problem setup. In the following one, we present our original contribution by offering an exhaustive analysis of the flow during a ramp-up motion at $Re_c = 2 \times 10^4$. Finally, the last section summarizes our main findings and draws some conclusions.

2. Numerical formulation

To tackle the problem at hand, we consider an incompressible three-dimensional unsteady flow field, around a straight wing with an infinite spanwise dimension as sketched in Figure (1a). The chosen coordinate system is a Cartesian inertial one, with the x and y axis (x_1 and x_2) aligned with the parallel and normal to the airfoil chord directions, while z (x_3) is the axis normal to the paper. Also, u , v and w (u_1 , u_2 and u_3) are used to denote the velocity components parallel and normal to the chord, and along the span respectively. With the given notations, using Einstein's summation convention, the dimensionless equations that govern the incompressible flow motion are:

$$\frac{\partial u_i}{\partial t} + \frac{\partial u_i u_j}{\partial x_j} = -\frac{\partial P}{\partial x_i} + \frac{1}{Re_c} \frac{\partial^2 u_i}{\partial x_j \partial x_j} + f_i, \quad (1)$$

$$\frac{\partial u_i}{\partial x_i} = 0, \quad (2)$$

The equations given above, have been made non-dimensional using the magnitude of the free stream velocity U_∞ and the airfoil chord c . Also, in the momentum Equation (1), $Re_c = U_\infty c / \nu$ is the chord-based Reynolds number and f_i represents a system of singular body forces used to keep into account the presence of the flap as it will be discussed later.

The momentum and mass conservation equations (1 and 2), are discretised on a cell-centered, co-located grid using a well-established curvilinear finite volume code [21, 33, 34]. The fluxes are approximated by a second-order central formulation, and the method of Rhie and Chow [35] is used to avoid spurious pressure oscillations. The equations are advanced in time by a second-order semi-implicit fractional-step procedure [36], where the implicit Crank-Nicolson scheme is used for the wall normal diffusive terms, and the explicit Adams-Bashforth scheme is

employed for all the other terms. The pressure Poisson equation arising when imposing the solenoidal condition on the velocity field, is transformed into a series of two-dimensional Helmholtz equations in wave number space via Fast Fourier transform (FFT) in the spanwise direction. Each of the resultant elliptic $2D$ problem is then solved using a preconditioned Krylov method (PETSc library [37]). In particular, the iterative Biconjugate Gradient Stabilized (BiCGStab) method preconditioned by an algebraic multigrid preconditioner (boomerAMG) [38] revealed to be quite efficient in dealing with the decoupled elliptic problems. The code is parallelized using a streamwise domain decomposition via the MPI message passing library. Further details on the code, its parallelization and the extensive validation campaign that has been carried out in the past can be found in Rosti et al. [21].

The aerofoil that has been selected for the present study is a symmetric NACA0020, which has been extensively studied in static stalled conditions by the authors in a previous research [21]. The flow domain around the aerofoil is meshed using a body fitted C grid arrangement (see Figure (1b)). The grid is adapted to the three dimensional case by uniformly repeating the baseline $2D$ grid in the spanwise direction. The boundary conditions that have been considered are as follows. Impermeability and no slip conditions are set on the aerofoil wall, periodic conditions are enforced on the planes bounding the domain in the spanwise direction, and continuity of the flow variables is applied through the top and bottom planes generated by the C-grid topology downstream of the trailing edge. On the external surface that bounds the computational domain, a convective boundary condition is used for the outlet, while a Dirichlet type condition based on an far-field irrotational approximation (Hess and Smith panel method [39]) of the flow is enforced on the inlet portion of the surface bounding the computational domain.

When a dynamic variation of the angle of incidence is considered, as in the ramp-up case, the inlet conditions are modified accordingly by changing the local direction of the velocity vector. An alternative formulation to impose the ramp-up manoeuvre, consisting in rotating the aerofoil in time using a non-inertial frame of reference mounted on the wing [40] (axis of rotation passing through the centroid of the foil), has also been considered. Before discarding this last option, we have evaluated the difference in the results obtained when using the two approaches. No significant differences have been observed when low reduced frequencies are considered and the rotation takes place along an axis normal to the paper passing through the centroid of the aerofoil. In particular, the variation in the lift and drag integral values revealed to be quite marginal.

Thus, all the three-dimensional simulations that will be presented have been obtained considering an inertial frame of reference, at a chord Reynolds number $Re_c = 20000$ and by varying the angle of attack according to a ramp function of time with an initial linear increase (constant rate $k = 0.12U_\infty/c$) from 0 to 20° and a subsequent constant value of the angle of attack, kept at $\alpha = 20^\circ$ (stalled condition).

The grid system that has been chosen for the three-dimensional simulations, has been determined after a number of trial-and-error tests and companion grid convergence studies spanning the whole free stream velocity vector rotation. Finally, we have selected a $2785 \times 626 \times 97$ (nodes in the x_1 , x_2 and x_3 directions, respectively) grid. In terms of local wall units, in the turbulent portion of the attached boundary layer, the corresponding mesh resolution verifies $\Delta x^+ < 3.0$, $\Delta y^+ < 0.5$ and $\Delta z^+ < 7.5$ (superscript $+$ indicates standard local viscous units lengths: i.e., lengths made non dimensional using the kinematic viscosity ν , and the skin friction velocity u_τ). Further details on the procedure that has been followed to generate the grid and the mesh refinement study campaign can be found in [21].

The conceptual aerofoil-flap configuration that has been considered is sketched in Figure (1c) showing the NACA0020 aerofoil with a rigid thin flap hinged via a torsional spring in the trailing edge region. The flap motion takes place in the x - y plane (i.e., no torsion allowed around their main axis), and is modelled using the second order ordinary differential equation

$$I\ddot{\theta} + C\dot{\theta} + K\theta = \mathcal{T} \quad (3)$$

In equation (3), θ is the angular displacement with respect to the equilibrium angle (i.e, $\theta = 0$) assumed to correspond to the condition in which the flap is tangent to the aerofoil. Also, I is the flap moment of inertia, C and K are the spring damping factor and stiffness, while \mathcal{T} is the torque exerted by the fluid on the flap.

The fluid-solid coupling of the moving appendages is kept into account by a singular body force distribution discretely applied along the flaps. This discrete, localised force system corresponds to the forces f_i appearing in the momentum equation (Equation (1)), and the integral of their moments about the flap hinge constitutes the torque term \mathcal{T} in (3). The intensity of the body forces f_i is related to the correct imposition of zero relative fluid velocity on the flaps. In particular, their values are determined by the immersed-boundary RKPM method [41] supposing a zero thickness flap. Further details on the implementation of the present fluid-structure interaction methodology using the IB-RKPM method on moving and/or deformable slender bodies are given in Favier et al. [42].

3. Results and discussions

To introduce the effects produced by the presence of a membrane-like flap hinged on the suction side of an aerofoil, we first illustrate the main features of the baseline flow under consideration: the flow around a NACA0020 aerofoil undergoing a ramp-up manoeuvre without the application of any control device at a chord Reynolds number fixed to the value of $Re_c = 2 \times 10^4$. In particular, the angle of attack undergoes an initial linear increase from $\alpha = 0$ to $\alpha = 20^\circ$ with a reduced frequency $k = 0.12U_\infty/c$ followed by a steady value of the angle at $\alpha = 20^\circ$. The variation of α with time matches the experimental conditions of Brucker and Weidner [6] and is also very similar to the one considered in [5].

3.1. Baseline flow description

All the ramp-up simulations are initialized from a fully developed, zero degree angle of attack flow condition. All averaged quantities that will be presented have been obtained employing a double averaging procedure: space averaging in the homogeneous z -direction and ensemble averaging at same time instants obtained from simulations using different initial conditions. In particular, similarly to Rosti et al. [21], we have considered ten realisations obtained using ten different initial conditions obtained from instantaneous zero degree flow fields sampled within two shedding cycles.

Figure (2a) shows the time evolution of the lift and drag coefficients during the ramp-up motion for the baseline configuration without flap (solid lines) (see Rosti et al. [21] for further details). Initially, both coefficients increase until reaching their maximum values well after the end of the linear increase of the angle of attack. At about $5tU_\infty/c$, the lift decreases abruptly while the drag starts to diminish at a later time. As it will be described later on, the drop in the force coefficients,

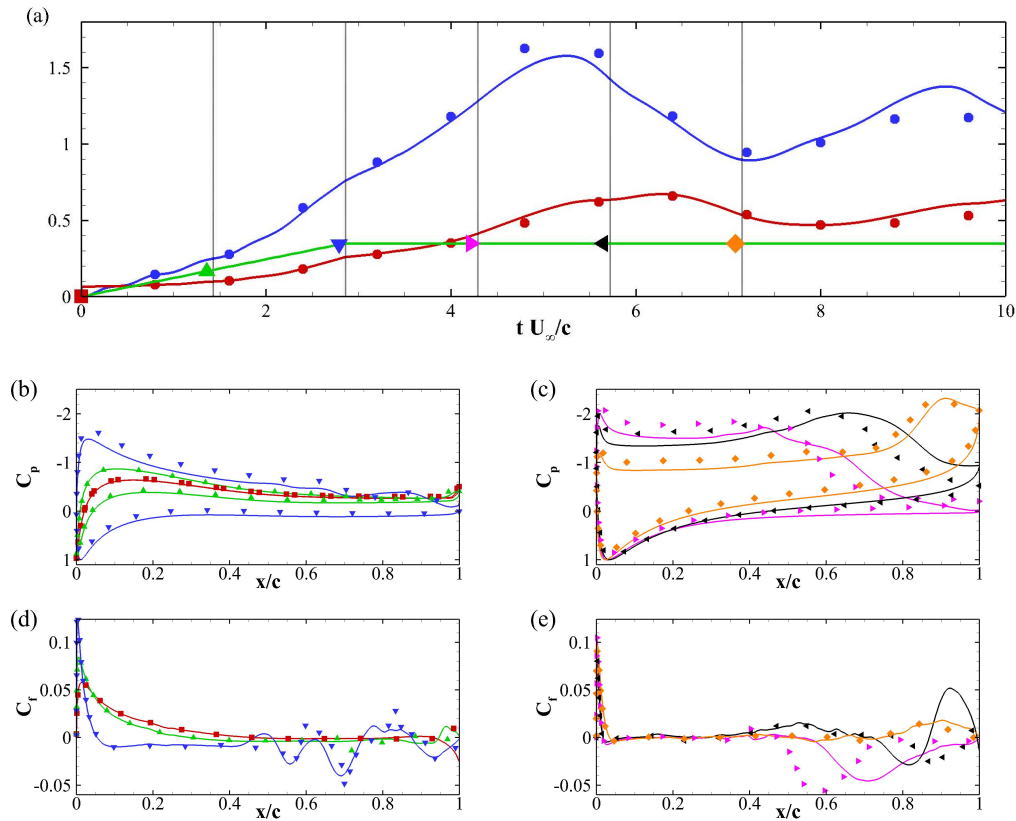


Figure 2. (a) Lift (blue line) and drag (red line) coefficients as a function of time. The green line is representative of the time variation of the angle of attack. Along this last line, the symbols indicate 6 particular time instants for which integral quantities along the aerofoil are represented in the remaining panels of the figure. In these diagrams, solid continuous lines represent the baseline cases while the symbols are for the cases of the aerofoil equipped with the flap. Also the colours indicate the time level at which the information has been extracted (consistently with the colours of the top panel). (b)-(c) Pressure coefficient C_p and (d)-(e) friction coefficient C_f at the selected times.

is related to the detachment of the dynamic stall vortex from the aerofoil. At a later time, the integral forces oscillate slowly converging towards the asymptotic static-stall values, in agreement with the physical description given by McCroskey [2]. During their time evolution, the maximum values achieved by the lift and drag coefficients are $C_L = 1.58$ and $C_D = 0.67$, respectively. Both these values are about the double of the corresponding coefficients measured in the static case at $\alpha = 20^\circ$ (see Rosti et al. [21]).

The other panels of Figure (2) show the time evolution of the pressure coefficients C_p (b and c) and of the friction coefficients C_f (d and e). Figure (3) displays the contours of the span-wise, z -component of vorticity ω_z , averaged in the homogeneous z -direction at the same six times as the ones considered in Figure (2). In particular, the first plot corresponds to the zero degree angle of attack, the second to $\alpha = 10^\circ$ and the others at various time instants at $\alpha = 20^\circ$. Figure (3a) shows how the flow is mostly symmetric over the aerofoil surface when $\alpha = 0^\circ$. Consistently, also the C_p distribution appears to be symmetric (Figure (2b)), with a plateau starting at about the mid-chord position, indicating the presence of a separated region. The presence of the separated flow appears clearly from the friction coefficient distribution (Figure (2d)) that presents a peak near the leading edge, followed by a smooth decrease and a separation point at about the mid-chord location. As the angle of attack is increased, the pressure distribution (Figure (2b)) and the flow field (Figure (3b-c)) loose their symmetry with a consequent lift increase. At increased angles of attack, the maximum friction coefficient and the

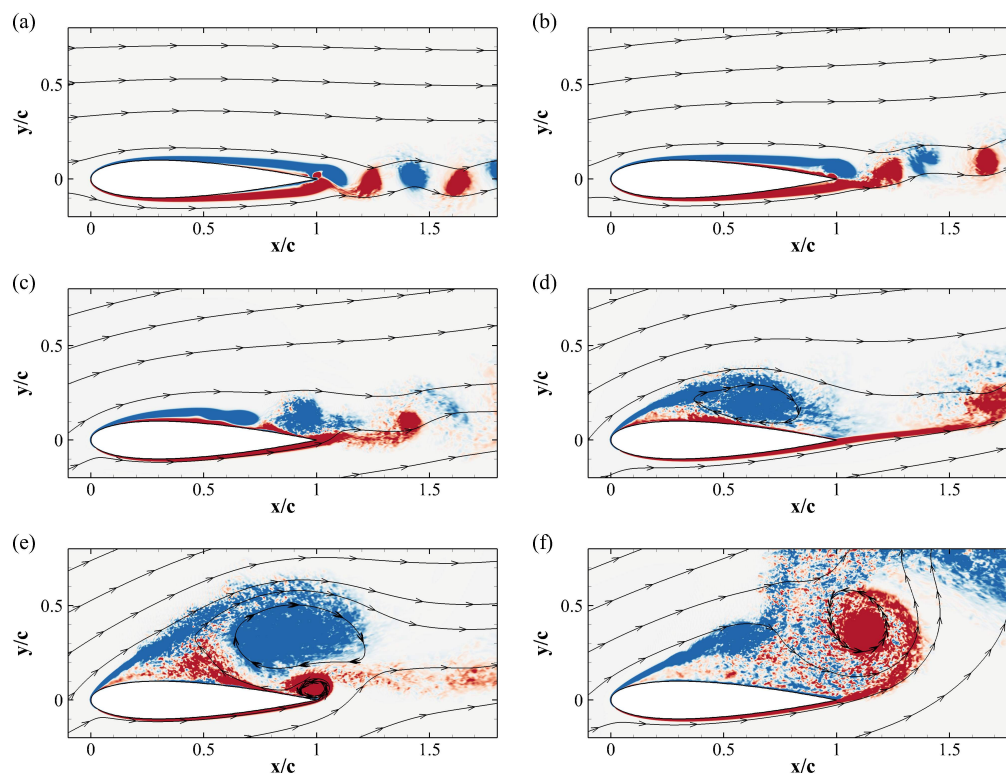


Figure 3. Contour plots of the space and ensemble average of the spanwise component of vorticity ω_z of the baseline simulation. The contours plots have been obtained at the times indicated in Figure (2a). Blue negative vorticity, red positive ($\pm 7U_\infty/c$).

separation point move towards the leading edge (Figure (2d)). Even after having reached the maximum incidence, the lift coefficient keeps increasing (Figure (2a)) with a pressure coefficient distribution that does not show the typical separation plateau [21]. As the peak of the pressure near the leading-edge is still increasing, and a second peak appears around the mid-chord (Figure (2c)). The latter is the footprint of a large vortex which has started to form on the suction side (i.e., the so called dynamic stall vortex), see Figure (3d). It is also noted that until the maximum lift is not reached, no vortices are shed from the trailing edge as can be educed from Figure (3d). After its formation, the dynamic stall vortex is convected downstream towards the trailing edge (as indicated by the displacement of the second pressure peak in Figure (2c)), where an induced counter rotating vortex is formed, see Figure (3e). When the dynamic stall vortex finally detaches from the aerofoil and the trailing edge vortex reaches its maximum size (Figure (3f)), the pressure attains an almost constant distribution indicating a fully separated flow condition (Figure (2c)). The complete time evolution of the separation point is reported by the solid line in Figure (4a). At $\alpha = 0^\circ$ the separation point is located at $x_s = 0.47c$, moving towards the leading edge as the angle of attack is increased. As already remarked, the static stall separation point $x_s = 0.025c$ (dashed line) is firstly reached when the ramp-up motion is finalised at $t = 3.5c/U_\infty$. In the subsequent stage, when the incidence angle is constant ($\alpha = 20^\circ$), the separation line moves further upstream followed by a damped oscillating positioning around its static value.

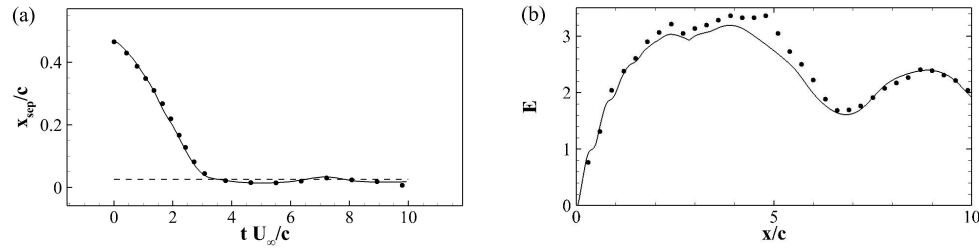


Figure 4. Time evolutions of the (a) downstream separation point and (b) aerodynamic efficiency $E = C_L/C_D$ during the ramp-up manoeuvre. Solid lines and symbols are used for the baseline and controlled cases, respectively. The dashed line in (a) represents the separation point at 20° .

3.2. Hinged flap: parametric study

We now turn our attention to the effects of a membrane-like flap mounted on the suction side of the aerofoil during the same ramp-up motion. As an initial step, we had to identify a design of the flap able to deliver substantial aerodynamic benefits during the manoeuvre. A proper design must keep into account that the flap motion and its effects on the flow field are controlled by various parameters, such as its length, inertia, position, the torsional spring stiffness and its damping factor. In a previous study, focusing on stall at fixed angle of attack (at $\alpha = 20^\circ$), we have carried out a parametric study aimed to identify an optimal control condition defined as the one that delivers the highest lift coefficient C_L while preserving or improving the aerodynamic efficiency $E = C_L/C_D$ (see [32]). For the present study, where the incidence varies with time, we proceed with a similar parametric study but pursuing a different aerodynamic condition. In particular, we define as a desired condition the one that maintains high efficiency during all the manoeuvre, postpones the dynamic stall, i.e., the lift breakdown, and reduces the subsequent degradation rate of the lift coefficient. Table (1) details all the flap configurations that have been considered. In particular, apart from the baseline case without flap, we have analysed flap lengths in the range $L/c = 0.1 - 0.3$, and spring stiffnesses in the range $K = 0.037 - 0.600$. Note that the spring stiffness can be related to the natural frequency of the flap as $K = I(2\pi f)^2$, where I is the moment of inertia with respect to the rotation axis given by $I = mL^2/3$, (m being the mass per unit spanwise length). The chosen stiffness values correspond to flap natural frequencies ranging between the half and the double of the shedding frequency of the baseline foil at the maximum angle of attack achieved in the ramp-up motion, i.e., $f_0 = 0.58U_\infty/c$ at $\alpha = 20^\circ$. In previous studies (see [31] and [32]), we have also analysed both the effects of the flap hinge position, and of a different configuration consisting of two flaps positioned in tandem on the suction side of the aerofoil. The effect of these parameters has not been considered in this study, since it was found that the aerodynamic performances were not very sensitive to their introduction. Having considered all the cases reported in Table (1), we have found that the best performance is achieved when using a flap $0.1c$ long, resonating with the shedding frequency of the uncontrolled aerofoil at an incidence of $\alpha = 20^\circ$. A summary of the time evolution of the lift coefficients during the ramp-up manoeuvre obtained using various flap configurations is reported in Figure (5) (note that, only the lift breakdown phase is shown in the figure).

3.3. Flow around the foil equipped with the selected flap

In this section we will be focusing on the aerodynamic performances and on the flow field generated around a NACA0020 aerofoil equipped with a zero thickness flap mounted on its suction side during the ramp-up motion under consideration. The

Case	f/f_0	L/c	x_F/c	$K \times 10^3$	$I \times 10^3$
Ref	—	—	—	—	—
F0.25-L0.10-X0.7	0.25	0.10	0.7	2.3461	3.3333
F0.50-L0.10-X0.7	0.50	0.10	0.7	9.3847	3.3333
F1.00-L0.10-X0.7	1.00	0.10	0.7	37.539	3.3333
F2.00-L0.10-X0.7	2.00	0.10	0.7	150.15	3.3333
F4.00-L0.10-X0.7	4.00	0.10	0.7	600.62	3.3333
F0.25-L0.20-X0.7	0.25	0.20	0.7	9.3847	13.333
F0.50-L0.20-X0.7	0.50	0.20	0.7	37.539	13.333
F1.00-L0.20-X0.7	1.00	0.20	0.7	150.15	13.333
F2.00-L0.20-X0.7	2.00	0.20	0.7	600.62	13.333
F4.00-L0.20-X0.7	4.00	0.20	0.7	2402.5	13.333
F0.25-L0.30-X0.7	0.25	0.30	0.7	21.115	30.000
F0.50-L0.30-X0.7	0.50	0.30	0.7	84.462	30.000
F1.00-L0.30-X0.7	1.00	0.30	0.7	337.85	30.000
F2.00-L0.30-X0.7	2.00	0.30	0.7	1351.4	30.000
F4.00-L0.30-X0.7	4.00	0.30	0.7	5405.6	30.000

Table 1. Flap configurations considered in the parametric study. The aerofoil is NACA0020 and the Reynolds number is $Re_c = 20000$. The flap parameters, i.e., the ratio between the spring natural frequency and the shedding frequency f/f_0 , the flap's length L , the hinge position x_F , the spring rotational stiffness K , and the moment of inertia I are provided.

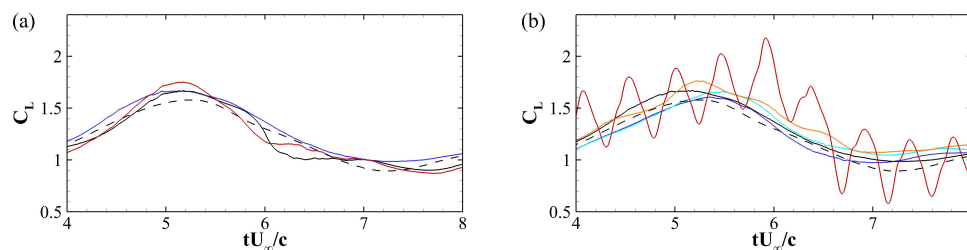


Figure 5. Evolution of the lift C_L for some of the cases considered in the parametric study. In panel (a), the length of the flap is varied, while keeping the flap natural frequency equal to the foil shedding frequency. The blue, black and red lines are used to identify the lift coefficients obtained with flap lengths equal to $L = 0.1c$, $0.2c$ and $0.3c$, respectively. In panel (b) we consider cases where the length of the flap is frozen to $L = 0.1c$, and the natural frequency of the flap is changed; the blue, light blue, black, orange and red lines are used for $f = 0.25f_0$, $0.5f_0$, $1.0f_0$, $2.0f_0$ and $4.0f_0$, respectively (f_0 being the shedding frequency of the baseline foil at 20° incidence). The dashed line is used to indicate the reference cases.

chosen flap configuration corresponds to the one delivering the best performances as determined via the parametric campaign described in the previous section: flap length $0.1c$, hinged at $0.7c$, infinitely long in the spanwise direction, and with a torsional stiffness adjusted to produce a flap natural frequency matching f_0 (the shedding frequency of the baseline profile at 20° incidence). For convenience, in what follows the aerofoil equipped with the aforementioned, quasi-optimal flap will be simply termed either as the *controlled aerofoil*, or the *aerofoil with the flap*. A comparison of the time evolution of the lift and drag coefficients of the baseline aerofoil (continuous line) versus the controlled one (dotted line) during the ramp-up motion is displayed in Figure (2). From the diagram, it appears that the drag coefficient C_D is only slightly influenced by the presence of the flap, while the lift coefficient C_L is increased during the initial $7tU_\infty/c$ time units, thus indicating an overall increase in aerodynamic efficiency E during the ramp-up motion. Figure (4b) reports the time variations of the aerodynamic efficiency E (defined as the ratio between the lift and drag coefficients, i.e., $E = C_L/C_D$). The graph shows how the controlled case presents higher values of the efficiency than the baseline one during the whole manoeuvre, with a maximum which is approximately 10% higher than in the uncontrolled case. From the figure, it also appears that higher efficiency is also maintained during the whole lift breakdown phase. Moreover, in the most critical condition, the minimum lift coefficient at the end of the lift breakdown is sensibly higher (about 12%) in the controlled case than in the uncontrolled one (i.e., with flap: $C_L^{min} = 1.0$; baseline case: $C_L^{min} = 0.89$). Thus, when the flap is used, a less severe lift deficit following the dynamic stall

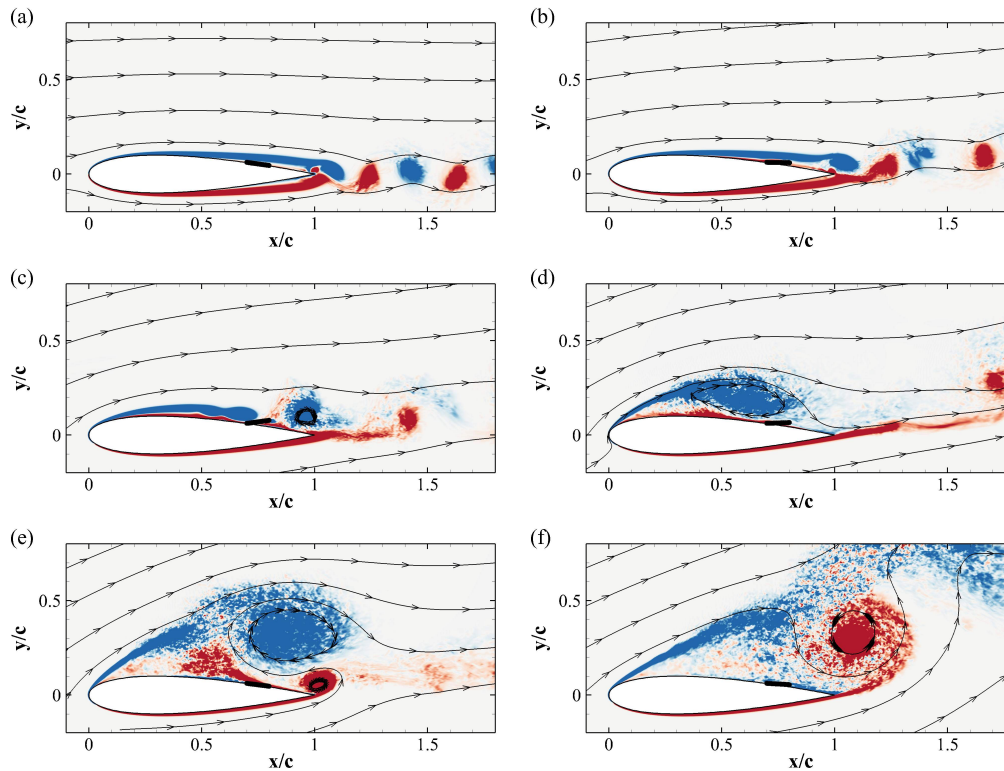


Figure 6. Contour plots of the space and ensemble average of the spanwise component of vorticity ω_z for the controlled case with flap, sampled at the times given in Figure (2a). Blue negative vorticity, red positive ($\pm 7U_\infty/c$).

overshoot delivers a smoother aerodynamic response to the unsteady change of incidence. The milder aerodynamic response induced by the presence of the flap is also enhanced by the extended time interval over which the lift decreases after the first lift maximum: in the controlled case this period of time is extended by 5% as compared to the baseline case.

Figure (6) shows the flow evolution during the ramp-up manoeuvre in terms of spatial and phased averaged spanwise vorticity when the flap is in use. The selected snapshots and vorticity levels correspond to the ones of the baseline case illustrated in Figure (3). Initially, at $\alpha = 0^\circ$, the flow is mostly attached to the aerofoil, and the flaplet lies tangentially on the aerofoil surface (Figure (6a)). As the angle of attack is increased and the separation point moves upstream (Figure (6b-c)), the flap starts to lift reducing the backflow advancing from the trailing edge. Within this stage, the pressure coefficient C_p (Figure (2b)) of the controlled case shows a higher leading edge pressure peak. It is also noted that the presence of the flap postpones the C_f oscillations (see Figure (2d)). In the following stage, when the dynamic stall vortex is forming and maximum lift is almost reached (Figure (6c-e)), the flap reverses his movement, now directing towards the wing surface. The flap downward motion generates a jet that displaces the forming trailing edge vortex downstream. This flap-flow interaction process delays the detachment of the dynamic stall vortex, resulting in a higher maximum lift value (maximum value in the controlled case: $C_L^{max} = 1.68$), and in a milder lift breakdown. A footprint of the same process can also be observed in the C_p and C_f distributions in Figure (2c,e) that show how the second pressure peak and the friction oscillations due the movement of the dynamic stall vortex occur at a chord location closer to the leading edge. Differently from the previous magnitudes, the time displacement of the mean separation point over the suction side, shown in Figure (4a), is only slightly altered

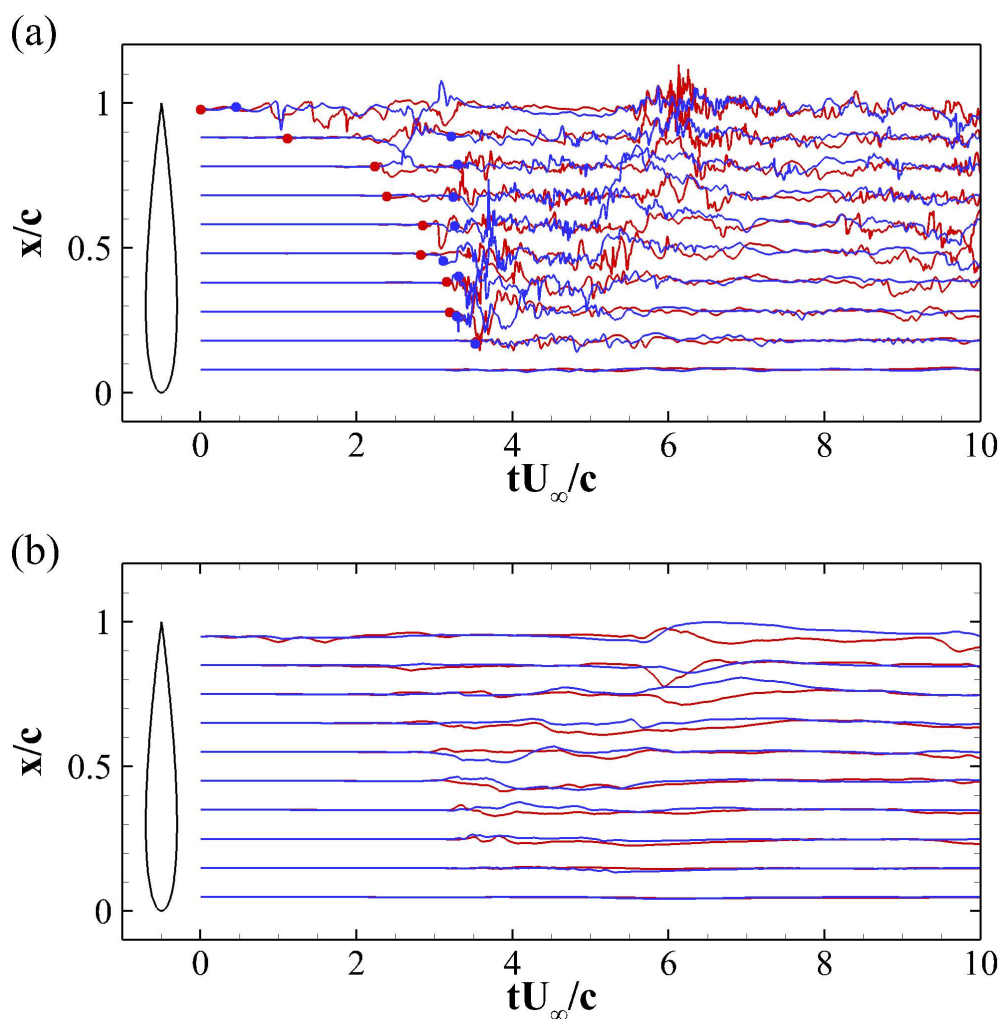


Figure 7. Fluctuations of the (a) x -velocity components u' and (b) pressure p as a function of time for various points near the aerofoil surface. For clarity, the fluctuations are shifted according to the chord location where they were measured. Red lines are for the baseline case, blue lines are for the aerofoil with the flap. For further explanations see the text

by the presence of the flap.

When describing Figure (2d-e), we have already highlighted the presence of some oscillations in the C_f distribution by the trailing edge region. These oscillations amplify in time thus affecting larger portions of the foil. The physical mechanism responsible for these oscillations is a shear layer instability of Kelvin-Helmholtz type that originates from the trailing edge and propagates upstream in time. The time-space propagation of this instability is analysed in Figure (7a) that shows the evolution over time of the fluctuations of the stream-wise velocity component at various x locations at a wall normal distance of $0.1c$ above the aerofoil suction side. The red and blue curves are used for the baseline and controlled cases, respectively. The symbols in the same figure indicate the time when the amplitude of the fluctuation reaches 2.5% of the averaged streamwise velocity value. In this diagram it is clear that in the baseline case initially the x -wise velocity fluctuations are confined to the trailing edge region and that only after 2 time units the fluctuations reach the half chord location. At a later stage, the fluctuations travel slowly further upstream, but never contaminating the leading edge portion of the aerofoil. This behaviour proves that in the baseline case, during the ramp-up motion, the separated region travels upstream from the trailing edge. When the flap

x/c	0.1	0.2	0.3	0.4	0.5	0.6	0.7	0.8	0.9	1.0
u' %	0	0	-1	-1	-1	-6	-10	-10	-12	-8
p' %	3	2	2	1	0	-5	-15	-25	-21	-20

Table 2. Percentage variations of the r.m.s. values of the streamwise velocity component and pressure fluctuations in the aerofoil with flap with respect to the baseline foil. The locations x/c are the same as the ones Figure (7)

is considered, the situation is quite different. In this case, the locations upstream of the flap hinge are reached by the perturbations with a slight time delay, while the the fluctuations downstream of the hinge are strongly reduced in amplitude and postponed in time. Table (2) confirms the aforementioned effect of the flap in reducing the velocity fluctuations in the rear part of the aerofoil (by approximately 10%) while leaving the intensity of the fluctuations almost unchanged in the front part.

Figure (7b) and Table (2) also illustrate the behaviour of the pressure fluctuations that further highlights the difference between the two cases with a maximum reduction of pressure rms of about 25% at 80% of the chord.

Further insight into the physical processes taking place during the ramp-up motion can be gained by analysing the time emergence of coherent structures, their mutual interactions and the generation of the wake. In particular, vortical coherent structures have been identified using the \mathcal{Q} -criterion proposed by Hunt et al. [43]. This technique allocates a vortex to all spatial regions that verify the condition

$$\mathcal{Q} = \frac{1}{2} (|\boldsymbol{\Omega}|^2 - |\boldsymbol{S}|^2) > 0, \quad (4)$$

where $\boldsymbol{S} = \frac{1}{2} (\nabla \boldsymbol{u} + \nabla \boldsymbol{u}^T)$ is the rate of strain tensor and $\boldsymbol{\Omega} = \frac{1}{2} (\nabla \boldsymbol{u} - \nabla \boldsymbol{u}^T)$ is the vorticity tensor. Instantaneous \mathcal{Q} iso-surfaces are shown in Figure (8). The left column corresponds to the baseline profile, while the right one presents the case of the aerofoil with the flap. The rows in the figure have been captured at the same time after the beginning of the ramp-up motion. Panels in the first row (a and b) correspond to the earliest stages at $t = 1.45c/U_\infty$, when the angle of attack is $\alpha = 10^\circ$. The flow is very similar in the two cases presenting a slight asymmetry, with coherent structures generated only past the trailing edge area of the suction side. At $\alpha = 20^\circ$ (panels c and d), the shear layer rolls-up into a recirculating region that closes at about the mid-chord location. However, the size and intensity of the large roller is strongly reduced when the flap is in use. Moreover in the controlled case, the whole shear layer instability and the consequent roll-up appear to be shifted downstream indicating a time delay in the whole instability process. The next panels (e, f and g and h) show how the roll-up process continues to develop leading to the formation of a very large recirculating zone (i.e., the dynamic stall vortex) that basically covers all the foil suction side. Again, the recirculating region and its intensity seem to be diminished by the action of the flap that also delays the process in time. In the same panels, it is also possible to observe the presence of a trailing edge vortex that interacts with the dynamic stall vortex inducing an upward displacement of the latter. As compared to the baseline case, in the controlled case, the trailing edge vortex is also displaced downstream. When the trailing edge vortex is shed, the leading edge shear layer starts to roll-up again forming a new vortex (see panels i and j). The whole process is then cyclically repeated in time with the intensity of the fluctuations slowly damped out to reach asymptotically the final stationary stalled condition.

A further analysis that allows to better understand the unsteady vortex formation, the associated transport processes and the origin of the instabilities arising

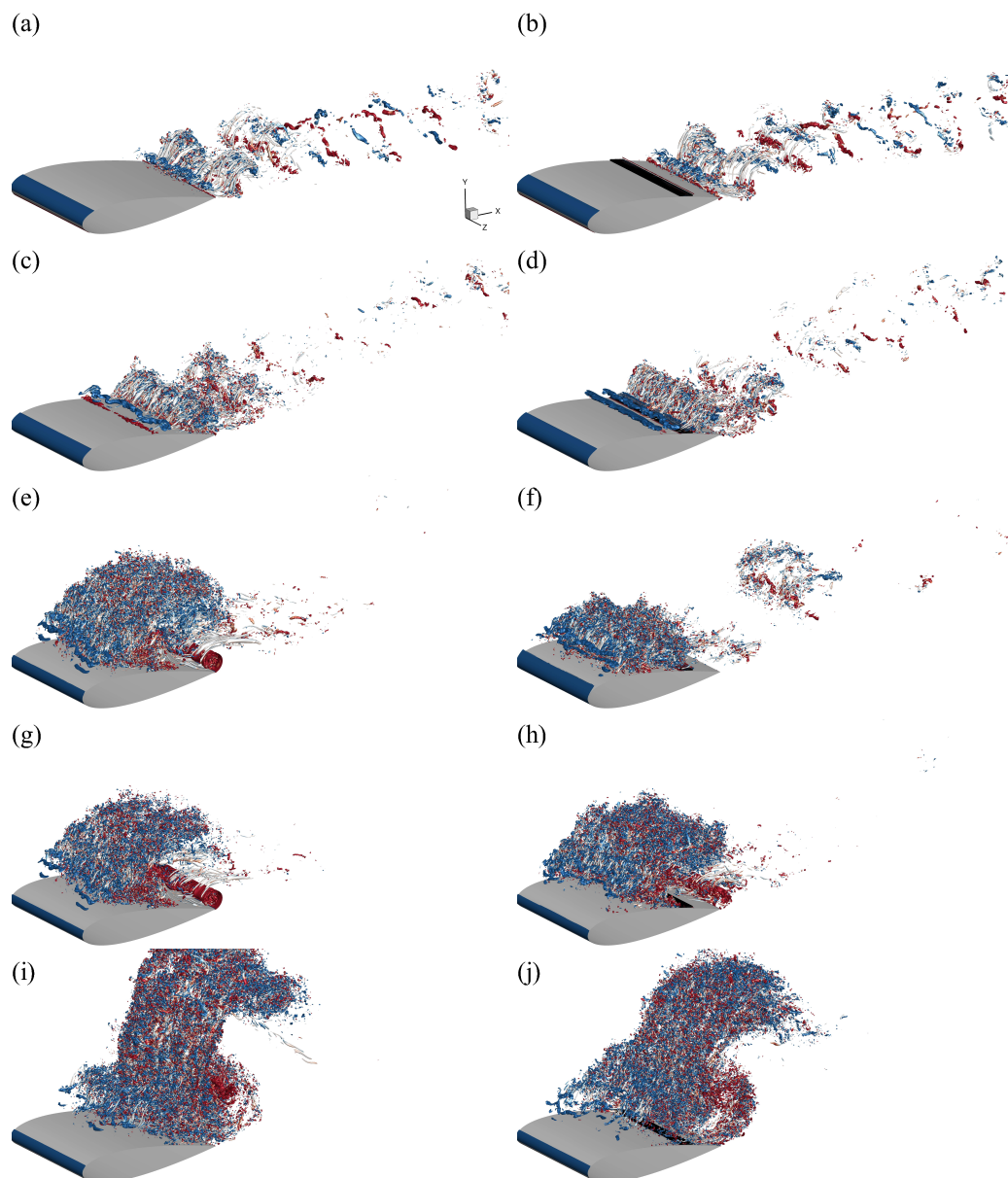


Figure 8. Visualisation of instantaneous vorticity field by means of Q -iso-surfaces ($Q = 500U_\infty^2/c^2$ for a-f and $Q = 1000U_\infty^2/c^2$ for g-j) coloured by the instantaneous spanwise component of the vorticity $\omega_z = \pm 40$ (red positive, blue negative). The left and right columns are used for the baseline and controlled cases, respectively.

in the flow is based on the study of the evolution of the Finite-Time Lyapunov Exponents (FTLE) [44, 45]. The FTLE, $\sigma^T(\mathbf{x}, t)$, is a scalar function of space and time which measures the rate of separation of neighbouring particle trajectories originating within a small ball centred at location \mathbf{x} and at time t . The FTLE over a given time interval $[t_0, t_0 + T]$ is defined as:

$$\sigma^T(\mathbf{x}, t) = \frac{1}{T} \ln \sqrt{\lambda_{max}(\Delta)}; \quad (5)$$

where Δ is the Cauchy-Green deformation tensor computed over the same finite

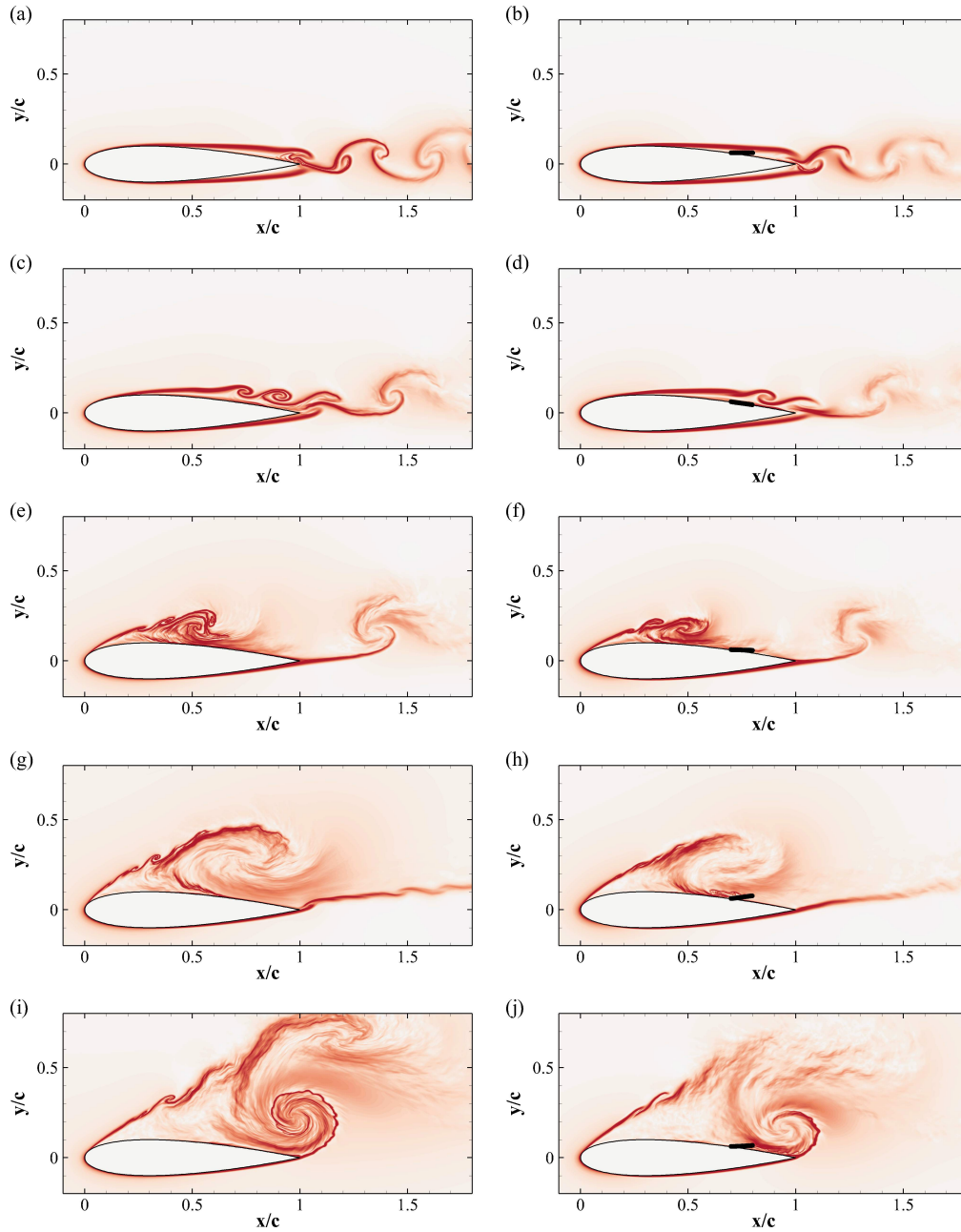


Figure 9. Contour plot of the FTLE σ^T . Time increases from top to bottom, with a sampling time interval of $\Delta t = 1.45c/U_\infty$. The initial time (a-b) corresponds to $\alpha = 10^\circ$. The contour levels go from 0 (white) to $7U_\infty/c$ (red). The left and right columns are used for the baseline and controlled cases, respectively.

time interval $[t_0, t_0 + T]$:

$$\Delta = \frac{\partial \mathbf{x}(t_0 + T, \mathbf{x}_0, t_0)}{\partial \mathbf{x}_0}. \quad (6)$$

The local extrema of the FLTE distribution are associated to the presence of coherent structures in the flow [45]. Figure (9) shows contours of the FTLE during a time period equal to the one considered in Figure (2). The frames are organised chronologically, with the left and right columns corresponding to the baseline and controlled cases, respectively. Starting from $t = 1.45c/U_\infty$, the snapshots have been extracted at the same time instants as the ones marked in Figure (2). In panels

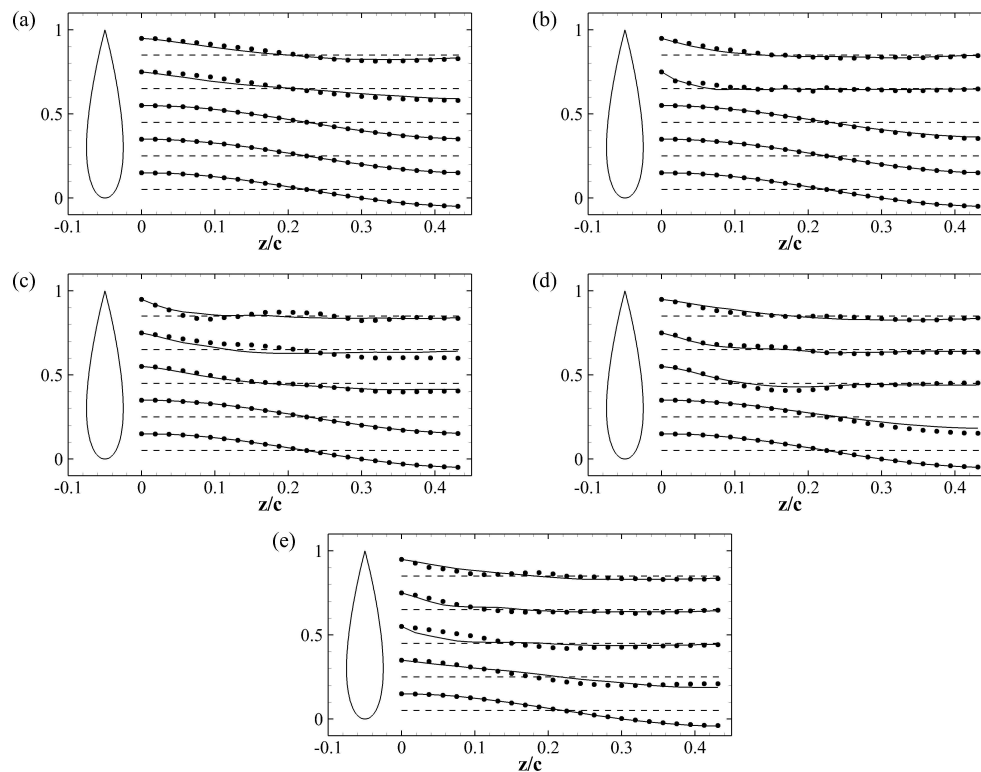


Figure 10. Spanwise pressure autocorrelation at various locations along the aerofoil suction side, computed at a distance of $0.1c$ from the wall. Time snapshots correspond to the ones given in Figure (2a). Solid line is the baseline case while symbols are for the case with flap.

a and b, the corresponding flow field is slightly asymmetric with two shear layers originating from the mid-chord region. The next two panels (b and c), show how the flow on the pressure side of the foil tends to reattach, while on the suction side an early separation is visible. Also, the shear layer at the trailing edge starts to roll up. As the shear layer roll-up process continues, a recirculation region is progressively built up on the foil suction side (see panel e and f), ultimately leading to the formation of a large scale vortical structure, i.e., the dynamic stall vortex. As already remarked when analysing Figure (8), the sequence of panels a-c-e and b-d-f show again that the action of the flap retards the roll up of the shear layers. It is also highlighted that, while the large scale, dynamic stall vortex is formed, no vortices are shed from the trailing edge and an almost stable straight shear layer develops from it. The last two panels (i and j) show how the trailing edge shear layer rolls-up forming a fresh trailing edge vortex which pushes the dynamic stall vortex upwards causing its detachment. From panel j it also appears that the action of the flap strongly delays the formation of the trailing edge vortex.

Finally, we analyse the spanwise two-point pressure autocorrelation R_{pp} at various xy coordinates. The autocorrelation is defined as

$$R_{pp}(z, r) = \frac{\overline{p'(z)p'(z+r)}}{\overline{p'^2(z)}}, \quad (7)$$

where the bar denotes the double average over time and along the homogeneous direction z . The pressure autocorrelation snapshots shown in Figure (10) have been extracted at the same time instants as those shown in Figure (2) that, in turn, correspond to the panels of Figure (8) and Figure (9). All the represented values have been obtained at a distance of $0.1c$ from the wall. In the first panel of Figure (10),

the flow is mostly attached to the aerofoil, and all the points are in the laminar region. A wake induced, low amplitude pressure wave (amplitude $\sim 0.3\%$ of the mean value) is visible at all the selected locations in panels a and b. In panel a, the controlled case shows the same behaviour except at the trailing edge, where the correlation reaches higher negative values. A more clear difference between the two cases is visible in panel b, that corresponds to the moment in which the angle of attack has reached 20° , and the separation point has moved upstream as shown in Figure (4a). In the baseline case the correlation rapidly goes to zero for all the points in the rear part of the aerofoil, indicating transition to turbulence. Differently, the case with flap maintains higher values of the autocorrelation function in all the region covered by the flap motion. In later stages (panels c and d), when the trailing edge vortex is starting to roll up, the baseline case takes on a higher value of the correlation function (see Figure (8e)). The lower value in the controlled case is due to the action of the flap that delays the formation of the trailing edge vortex. Finally in panel e, most of the correlation values are quite low, except in the region spanned by the flap motion (in the controlled case), where the correlation seems to grow again because of the coherent local flow motion induced by the flap movement.

4. Conclusion

The present numerical study focuses on the use of a passive, self actuated, zero thickness flap as a control device able to limit the abrupt lift breakdown typical of dynamic stall. In particular, we have considered a NACA0020 aerofoil undergoing a ramp-up manoeuvre (i.e., incidence angle α initially increasing linearly from 0° to 20° with a reduced frequency of $0.12U_\infty/c$, followed by a plateau at $\alpha = 20^\circ$) at a chord Reynolds number of 2×10^4 . After having conducted a detailed analysis of the baseline flow without flap, a number of different flap configurations have been considered having set as an aerodynamic objective one that: *i*) postpones the dynamic stall, *ii*) reduces the subsequent lift coefficient degradation rate and *iii*) delivers a high efficiency throughout the whole manoeuvre. In particular, we have considered a family of rigid, membrane-like flaps hinged at the same location on the foil suction side (i.e., 70% of the chord) via a torsional spring. Each different flap configuration, obtained by modifying the flap natural frequency (i.e., spring stiffness) and its length, has been evaluated in terms of the aforementioned criteria. Finally, it has been found that a flap measuring 10% of the chord, with a natural frequency matching the shedding frequency of the baseline foil at $\alpha = 20^\circ$ (in steady stalled conditions) delivers the best performances in term of the desired aerodynamic objectives. To shed some light on the physical mechanisms that improve the time evolution of the lift coefficient during the ramp-up motion, we have also systematically analysed the flow topology and its variations when the flap interacts with the fluid flow field. In general, it has been observed that already from the beginning of the linear increase of the incidence angle, the presence of the flap appears to delay the whole dynamic stall process. In particular, the flap retards the initial roll up process associated with the vorticity generated by the shear layer instability originating at the leading edge. This delay is also accompanied by a mitigating effect that decreases the intensity of the generated dynamic stall vortex. The latter, lifts up the flap during its passage thus partially inhibiting the interaction between the vortex advected along the suction side of the foil and the trailing edge shear layer that also appears to be stabilised by the flap action. The final flap downward motion also contributes to delay and to diminish the intensity of the trailing edge vortex. The described stages constitute a cycle that repeats in

time slowly reducing in intensity until the transient is completed and the steady angle of attack cyclic condition is recovered [21].

Acknowledgment

This research was partially funded by the EPSRC under grant EP/N020413 "Quiet Aerofoil of the Next Generation".

References

- [1] R.L. Halfman, H.C. Johnson, and S.M. Haley, *Evaluation of high-angle-of-attack aerodynamic-derivative data and stall-flutter prediction techniques*, , DTIC Document, 1951.
- [2] W.J. McCroskey, *The phenomenon of dynamic stall.*, , DTIC Document, 1981.
- [3] W.J. McCroskey, *Unsteady airfoils*, Annual review of fluid mechanics 14 (1982), pp. 285–311.
- [4] K. Mulleners, and M. Raffel, *The onset of dynamic stall revisited*, Experiments in fluids 52 (2012), pp. 779–793.
- [5] K. Mulleners, and M. Raffel, *Dynamic stall development*, Experiments in fluids 54 (2013), pp. 1–9.
- [6] C. Bruecker, and C. Weidner, *Influence of self-adaptive hairy flaps on the stall delay of an airfoil in ramp-up motion*, Journal of Fluids and Structures 47 (2014), pp. 31–40.
- [7] L.E. Ericsson, and J.P. Reding, *Fluid dynamics of unsteady separated flow. Part I. Bodies of revolution*, Progress in Aerospace Sciences 23 (1986), pp. 1–84.
- [8] L.E. Ericsson, and J.P. Reding, *Fluid dynamics of unsteady separated flow. Part II. Lifting surfaces*, Progress in Aerospace Sciences 24 (1987), pp. 249–356.
- [9] L.E. Ericsson, and J.P. Reding, *Fluid mechanics of dynamic stall part I. Unsteady flow concepts*, Journal of fluids and structures 2 (1988), pp. 1–33.
- [10] L.E. Ericsson, and J.P. Reding, *Fluid mechanics of dynamic stall part II. Prediction of full scale characteristics*, Journal of Fluids and Structures 2 (1988), pp. 113–143.
- [11] T. Lee, and P. Gerontakos, *Investigation of flow over an oscillating airfoil*, Journal of Fluid Mechanics 512 (2004), pp. 313–341.
- [12] C. Shih, L. Lourenco, L. Van Dommelen, and A. Krothapalli, *Unsteady flow past an airfoil pitching at a constant rate*, AIAA journal 30 (1992), pp. 1153–1161.
- [13] N.L. Sankar, and W. Tang, *Numerical solution of unsteady viscous flow past rotor sections*, AIAA paper 85 (1985), p. 5.
- [14] J.C. Wu, *A study of unsteady turbulent flow past airfoils*, Georgia Institute of Technology, 1988.
- [15] I.H. Tuncer, J.C. Wu, and C.M. Wang, *Theoretical and numerical studies of oscillating airfoils*, AIAA journal 28 (1990), pp. 1615–1624.
- [16] G.N. Barakos, and D. Drikakis, *Computational study of unsteady turbulent flows around oscillating and ramping aerofoils*, International journal for numerical methods in fluids 42 (2003), pp. 163–186.
- [17] S. Wang, D.B. Ingham, L. Ma, M. Pourkashanian, and Z. Tao, *Numerical investigations on dynamic stall of low Reynolds number flow around oscillating airfoils*, Computers & Fluids 39 (2010), pp. 1529–1541.
- [18] E. Dumlupinar, and V.R. Murthy, *Investigation of dynamic stall of airfoils and wings by CFD*, in *29th AIAA Applied Aerodynamics Conference* Curran, 2011, pp. 27–30.
- [19] K. Gharali, and D.A. Johnson, *Dynamic stall simulation of a pitching airfoil under unsteady freestream velocity*, Journal of Fluids and Structures 42 (2013), pp. 228–244.
- [20] J.A. Ekaterinaris, and M.F. Platzer, *Computational prediction of airfoil dynamic stall*, Progress in aerospace sciences 33 (1998), pp. 759–846.
- [21] M.E. Rosti, M. Omidyeganeh, and A. Pinelli, *Direct numerical simulation of the flow around an aerofoil in ramp-up motion*, Physics of Fluids 28 (2016), 025106.
- [22] T. Lee, and P. Gerontakos, *Dynamic stall flow control via a trailing-edge flap*, AIAA journal 44 (2006), pp. 469–480.
- [23] B. Heine, K. Mulleners, G. Joubert, and M. Raffel, *Dynamic stall control by passive disturbance generators*, AIAA journal 51 (2013), pp. 2086–2097.
- [24] D. Greenblatt, and I. Wygnanski, *Dynamic stall control by periodic excitation, Part 1: NACA 0015 parametric study*, Journal of Aircraft 38 (2001), pp. 430–438.
- [25] D. Greenblatt, and I. Wygnanski, *Effect of leading-edge curvature and slot geometry on dynamic stall control*, AIAA Paper 3271 (2002), p. 2002.
- [26] D. Bechert, M. Bruse, W. Hage, and R. Meyer, *Fluid mechanics of biological surfaces and their technological application*, Naturwissenschaften 87 (2000), pp. 157–171.
- [27] G. Bramesfeld, and M.D. Maughmer, *Experimental investigation of self-actuating, upper-surface, high-lift-enhancing effectors*, Journal of aircraft 39 (2002), pp. 120–124.
- [28] A.C. Carruthers, A.L.R. Thomas, and G.K. Taylor, *Automatic aeroelastic devices in the wings of a steppe eagle Aquila nipalensis*, Journal of Experimental Biology 210 (2007), pp. 4136–4149.
- [29] M. Schatz, T. Knacke, F. Thiele, R. Meyer, W. Hage, and D.W. Bechert, *Separation control by self-activated movable flaps*, AIAA Paper 1243 (2004), p. 2004.
- [30] J.U. Schluter, *Lift enhancement at low Reynolds numbers using self-activated movable flaps*, Journal of Aircraft 47 (2010), pp. 348–351.
- [31] M.E. Rosti, L. Kamps, C. Bruecker, M. Omidyeganeh, and A. Pinelli, *The PELskin project - part*

- V - Towards the control of the flow around aerofoils at high angle of attack using a self-activated deployable flap*, Meccanica (under review).
- [32] M.E. Rosti, M. Omidyeganeh, and A. Pinelli, *Passive control of the flow around an aerofoil using a flexible, self adaptive flaplet*, Journal of Fluid Mechanics (under review).
- [33] M. Omidyeganeh, and U. Piomelli, *Large-eddy simulation of three-dimensional dunes in a steady, unidirectional flow. Part 1. Turbulence statistics*, Journal of Fluid Mechanics 721 (2013), pp. 454–483.
- [34] M. Omidyeganeh, and U. Piomelli, *Large-eddy simulation of three-dimensional dunes in a steady, unidirectional flow. Part 2. Flow structures*, Journal of Fluid Mechanics 734 (2013), pp. 509–534.
- [35] C.M. Rhie, and W.L. Chow, *Numerical study of the turbulent flow past an airfoil with trailing edge separation*, AIAA journal 21 (1983), pp. 1525–1532.
- [36] J. Kim, and P. Moin, *Application of a fractional-step method to incompressible Navier-Stokes equations*, Journal of computational physics 59 (1985), pp. 308–323.
- [37] S. Balay, S. Abhyankar, M. Adams, J. Brown, P. Brune, K. Buschelman, L. Dalcin, V. Eijkhout, W. Gropp, D. Kaushik, M. Knepley, L.C. McInnes, K. Rupp, B. Smith, S. Zampini, and H. Zhang, PETSc Web page; <http://www.mcs.anl.gov/petsc>.
- [38] V.E. Henson, and U.M. Yang, *BoomerAMG: a parallel algebraic multigrid solver and preconditioner*, Applied Numerical Mathematics 41 (2002), pp. 155–177.
- [39] J.L. Hess, and A.M.O. Smith, *Calculation of potential flow about arbitrary bodies*, Progress in Aerospace Sciences 8 (1967), pp. 1–138.
- [40] J.G. Wong, A. Mohebbian, J. Kriegseis, and D.E. Rival, *Rapid flow separation for transient inflow conditions versus accelerating bodies: An investigation into their equivalency*, Journal of Fluids and Structures 40 (2013), pp. 257–268.
- [41] A. Pinelli, I.Z. Naqavi, U. Piomelli, and J. Favier, *Immersed-boundary methods for general finite-difference and finite-volume Navier–Stokes solvers*, Journal of Computational Physics 229 (2010), pp. 9073–9091.
- [42] J. Favier, A. Revell, and A. Pinelli, *A Lattice Boltzmann–Immersed Boundary method to simulate the fluid interaction with moving and slender flexible objects*, Journal of Computational Physics 261 (2014), pp. 145–161.
- [43] J.C.R. Hunt, A.A. Wray, and P. Moin, *Eddies, stream, and convergence zones in turbulent flows*, Center for turbulence research report CTR-S88 (1988), pp. 193–208.
- [44] G. Haller, *Distinguished material surfaces and coherent structures in three-dimensional fluid flows*, Physica D: Nonlinear Phenomena 149 (2001), pp. 248–277.
- [45] S.C. Shadden, F. Lekien, and J.E. Marsden, *Definition and properties of Lagrangian coherent structures from finite-time Lyapunov exponents in two-dimensional aperiodic flows*, Physica D: Nonlinear Phenomena 212 (2005), pp. 271–304.